# 4 The $Fe_4$ SMM class

## 4.1 Introduction

The slow magnetic relaxation properties of the family of $Fe_4$ molecules, conjugated with their chemical stability, made them one of the most interesting SMMs. Despite the low blocking temperature (hysteresis opening only below 1 K) $Fe_4$ molecules have been used as model systems to shed some light on the complex and fascinating behaviour of SMMs [1]. $Fe_4$ SMMs have the propeller like shape shown in fig. 4.1. In the archetypal $Fe_4$ system the three peripheral iron(III) ions are coordinated by two diketonate ligands, i.e. dipivaloylmethanate ($dpm^-$), while six μ-methoxide ($OMe^-$) anions bridge them to the central iron(III) ion to give the final formula $[Fe_4(OMe)_6(dpm)_6]$ [2]. The molecule is characterised by the presence of a $C_2$ symmetry axis passing through Fe1 and Fe2, thus the peripheral ions are arranged at the vertices of an isosceles triangle [2]. The antiferromagnetic coupling of the central ion ($s$=5/2) to the peripheral ones ($s$=3x5/2) causes the total spin of the ground state to be S=5. The ground state can be considered selectively populated for temperature below 5 K.

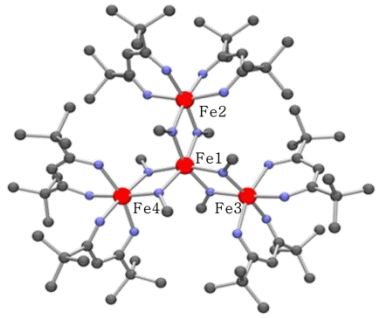


**Fig.4.1:** Molecular structure of the archetypal $Fe_4$ system, the $[Fe_4(OMe)_6(dpm)_6]$.

The degeneracy of the $S$=5 ground state is removed by the zero-field splitting Hamiltonian term:

$$H_{zfd} = D\left[\hat{S}_z^2 - \tfrac{1}{3}S(S+1)\right] \qquad (1)$$

where $D$, the axial anisotropy factor, is equal to $-0.2\ cm^{-1}$ for the $[Fe_4(OMe)_6(dpm)_6]$ and $\hat{S}_z$ is the projection of the total spin operator along the easy axis. Therefore the energy level as function of $m_s$, eigenvalues of $\hat{S}_z$ is a parabola (fig. 4.2).

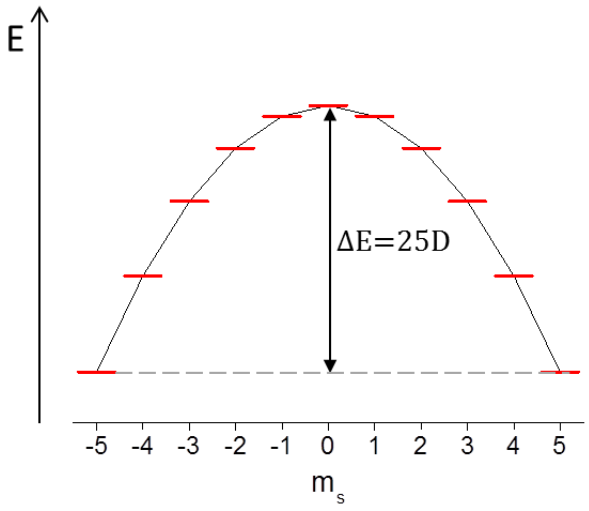


**Fig.4.2:** Energy level diagram of the $S$=5 state as function of the $m_s$ states in zero field; $\Delta E = DS^2$ is the energy of the anisotropy barrier.

The magnetic properties of the molecule, i.e. the $D$ parameter, can be easily tuned by replacing the six μ-metoxide bridges with two tripodal ligands, leading to the general formula $Fe_4(L)_2(dpm)_6$ [3,4]. The introduction of the tripodal ligands L=R-C$(CH_2OH)_3$ where R=Me, R=$CH_2$Br, R=Ph modifies the helical pitch of the Fe$(O_2Fe)_3$ unit toward three-fold symmetry. This also increases the axial anisotropy resulting in $D$ values equal to $-0.445\ cm^{-1}$, $-0.432\ cm^{-1}$, $-0.42\ cm^{-1}$, respectively [5]. The same trend is found also for the anisotropy barrier.

As in the case of the terbium(III) bis(phthalocyaninato) complex, the potential for the use of $Fe_4$ in spintronic devices, being one of the most stable and versatile SMM, boosted the development of its assembling strategies on surfaces [6]. The addition of sulphur-containing moieties on the R group of the tripodal ligands allowed the preparation of chemically grafted monolayers on gold surfaces. XMCD based experiments evidenced that the typical butterfly-shaped magnetic hysteresis of these SMMs was still observable in monolayers assembled on gold [7-9]. On the other hand the deposition from solution is still far from allowing a detailed characterisation of the film and a fine control of the molecular organization on surfaces. Indeed, the UHV thermal deposition, employed in this thesis for $TbPc_2$ SMMs, is highly desirable not only for the cleanness of the process but also for the possibility to control the coverage allowing also the investigation of individual molecules.

In order to exploit the UHV techniques physical deposition method based on the sublimation process is desirable. UHV sublimation allows a larger versatility in the selection of surfaces that can be used as well as a larger control of the deposition characteristics.

A considerable effort has been made to obtain SMMs that retain their properties after the thermal sublimation onto a surface. Among the several $Fe_4$, the complex bearing the tripodal ligand L=Ph-$C(CH_2OH)_3$ (hereafter $Fe_4Ph$, see fig. 4.3), has been proved to sublimate in UHV and to maintain its SMM character when deposited to form films a few hundreds nm thick. Although the SMM behaviour is preserved, both susceptibility and EPR measurements have shown the presence of some impurities (less than 5%) which can be associated with the very volatile $Fe(dpm)_3$ compound [10].

Starting from these findings one of the goals of this thesis has been the investigation of $Fe_4Ph$ at the single molecule level. STM and STS local probe techniques have been employed to characterise hybrid surfaces, i.e. $Fe_4Ph$ molecules sublimated on different surfaces. For this purpose XPS and UPS techniques were also employed to get important information about the chemical

composition and electronic properties of the molecular film. By means of a spectroscopic and STM characterisation we studied different kinds of hybrid surfaces ($Fe_4Ph$ on Au(111), Cu(100) and $Cu_2N$) succeeding in finding the suitable conditions to isolate the molecules on the surface and perform STS measurements.

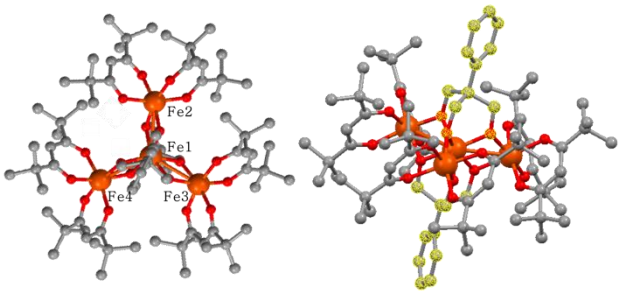


**Fig.4.3:** $Fe_4Ph$ structure; top view (left); side view (right), in yellow the atoms of the tripodal ligands.

## 4.2 Thick film characterisation

As a first step we looked for the optimal conditions for the UHV thermal deposition of $Fe_4Ph$. The molecule was synthetized by the group of prof. A. Cornia at the University of Modena and Reggio Emilia (UNIMORE) following the procedure already reported by our joined teams [5]. $Fe_4Ph$ crystals were mechanically ground before being inserted into the sublimation crucible. In order to define the parameters of the sublimation process a quartz crystal microbalance (QCM) was employed. For the microbalance calibration the crystal density of the $Fe_4Ph$, $\rho = 1.192\ g \cdot cm^{-3}$ [5], was used to evaluate the nominal thickness (see equation 2.13). The thickness values as a function of the time, while the crucible temperature is slowly increased, is reported in fig. 4.4. The sublimation rate becomes different from zero above 200 °C, as evidenced by the corresponding increase of the film thickness. These data are partially in contrast with previous experiments [10,11] where the sublimation rate is

reported to start at higher temperature; however the different experimental setup, in particular the thermocouple positioning, can account for this discrepancy.

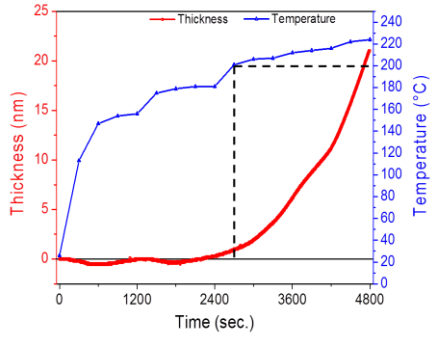


**Fig.4.4:** Quartz microbalance thickness data (red) and the corresponding temperature (blue) as a function of the elapsed time.

On the basis of QCM data, degassing of the powder has been carried out immediately below the sublimation temperature, i.e. 200°C maintaining this temperature for 48 hours before using it for the sample preparation. Then, every deposition was made by using a crucible temperature of 215°C, which allowed to have a very low nominal deposition rate (0.5Å/min). All $Fe_4$Ph films were prepared by keeping the substrate at room temperature. The sublimation process was then validated on the basis of the spectroscopic features (XPS and UPS) of a thick film (ca 4 nm) grown on the Au(111) surface.

The XPS spectra were acquired using a monochromatic Al $K_\alpha$ source (1486.6eV). The XPS spectra in the regions of interest (Fe *2p*, O *1s*, C *1s* and Au *4f*) and relative curve fitting are reported in fig. 4.5. The binding energy scale was calibrated by setting the Au $4f_{7/2}$ peak to 84.04 eV. The Fe *2p* region shows a typical structured signal due to the presence of satellite peaks. This region of the spectrum was fitted by using three components for each spin orbit peak, as reported in literature [12,13]. It is important to note that the binding energy of the first component of the Fe $2p_{3/2}$ peak is at 711.1 eV, in agreement with the expected value for $Fe^{3+}$ ions. Two components were used for the O *1s* region, in order to account for the shake-up peak. In the C *1s* region two contributions can be distinguished: a

main component due to aliphatic and aromatic carbon atoms (285.0 eV) and a shoulder due to the carbonyl and alcoholic carbon atoms (286.5 eV). The relative intensity of the two contributions matched the expected value of 3.8.

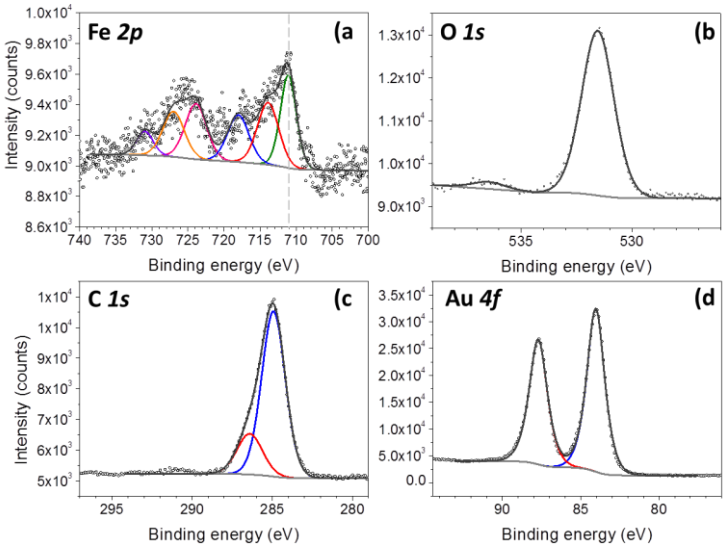


**Fig.4.5:** XPS data for the $Fe_4$Ph thick film (ca. 4 nm): Fe *2p* (a), O *1s* (b), C *1S* (c), and Au *4f* region (d) and their relative fits. The spectra were acquired using a monochromatic Al $K_\alpha$ source (1486.6eV).

In order to estimate abundance of each element percent the following formula were employed:

$$Fe\% = \frac{A_{Fe}/\sigma_{Fe}}{A_{Fe}/\sigma_{Fe}+A_C/\sigma_C+A_O/\sigma_O} \qquad (2)$$

$$C\% = \frac{A_C/\sigma_C}{A_{Fe}/\sigma_{Fe}+A_C/\sigma_C+A_O/\sigma_O} \qquad (3)$$

$$O\% = \frac{A_O/\sigma_O}{A_{Fe}/\sigma_{Fe}+A_C/\sigma_C+A_O/\sigma_O} \qquad (4)$$

Where$\Delta E$, $A_O$ and $A_C$ are the areas of Fe, O and C respectively and $\sigma_{Fe}$, $\sigma_O$, $\sigma_C$ their relative cross-section at 1486.6 eV. The good

agreement of the experimental data with the theoretical ones, suggests the presence of intact molecules on the surface (table 4.1).

| | Experimental | Expected |
|---|---|---|
| **Fe%** | 3.6 | 3.7 |
| **O%** | 16.8 | 16.7 |
| **C%** | 79.6 | 79.6 |

**Table 4.1:** Comparison between the expected elemental composition for $Fe_4Ph$ and that obtained by XPS analysis for a thick film of $Fe_4Ph$ (ca 4nm) grown on the Au(111) surface.

The spectroscopic characterisation of the film was completed by performing UPS experiments. By means of the He(II) source (40.8 eV), see section 2.4.2, it was possible to probe the occupied molecular states up to 20 eV below the Fermi level and thus to obtain a spectroscopic fingerprint of the molecule (green curve in fig. 4.6). The binding energy value ~2.6 eV of the highest molecular orbital (peaks 1,2) indicates the insulating character of the molecule which is an important aspect to take into account when correlating UPS with STM and STS measurements. The experimental spectrum (green curve) is in very good agreement with the theoretical DOS (red curve) calculated for the isolated molecule (see fig. 4.6).

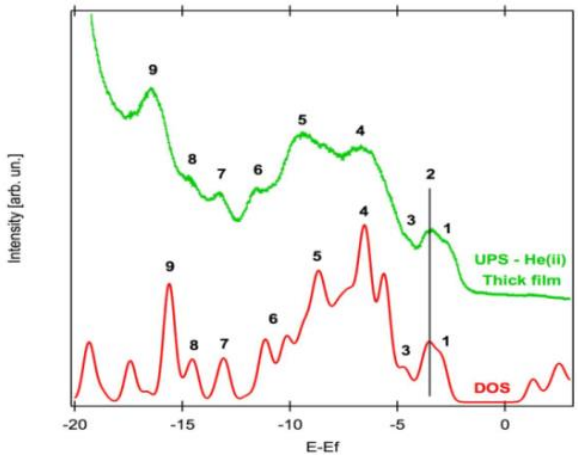


**Fig.4.6:**Comparison between the theoretical DOS calculated for the isolated $Fe_4Ph$ molecule and the UPS spectrum taken for a 4 nm $Fe_4Ph$ film deposited on Au(111).

All calculations were performed by S. Ninova with the CP2K program package [14] within the DFT framework and we provide here an overview of the calculations. Grimme's D3 parameterization

approach was used in order to introduce the dispersion correction term [15]. The revPBE [16] functional was chosen for the geometry optimization. The Norm-conserving Goedecker-Teter-Hutter (GTH) pseudopotentials were used together with GTH double-ζ polarized molecularly optimized basis sets for all atomic species [17]. An energy cut-off of 400 Ry was applied to the plane-wave basis sets. The $Fe_4Ph$ cluster was considered in its ground state (S=5), where the central ion is antiferromagnetically coupled with the peripheral ones. The size of the simulation cell was (25 x 25 x 25) Å. The structure of the $Fe_4Ph$ was taken from X-ray experimental data and it was geometrically optimized. For the density of states, the optimized structure was set to wavefunction optimization, using the hybrid functional PBE0 [18] and a 0.35 Gaussian convolution has been introduced in order to better compare with the experimental dataset. The theoretical spectrum has been shifted of about 2.8 eV in order to align the experimental and theoretical HOMO, the highest molecular orbital.

Both XPS and UPS investigations suggest the presence of intact molecules in the thermally deposited thick film. We then focused our attention on the preparation and characterisation of monolayer and sub-monolayer films, deposited on the Au(111) surface.

## 4.3 Preparation and XPS characterisation of $Fe_4Ph$ deposited on Au(111) at low coverage

In order to obtain the suitable coverage to study the molecule in isolated conditions (sub-monolayer deposition) we calibrated the evaporation times by referring to the XPS Fe *2p* signal of chemical grafted monolayer of $Fe_4C_9$ on gold [8]. The $Fe_4C_9$ belongs to the family of $Fe_4L_2dpm_6$ in which the tripodal ligands bear a sulphur moiety able to graft the molecule on the gold substrate. In this case $C_9$ stands for 11-(acetylthio)-2,2-bis(hydroxymethyl)undecan-1-ol. The gold substrate (100 nm Au/Mica) was left incubating for 24 hr in

a solution of 2 mM $Fe_4C_9$ in $CH_2Cl_2$. After that the surface was washed several times with$CH_2Cl_2$ to remove the physisorbed material.

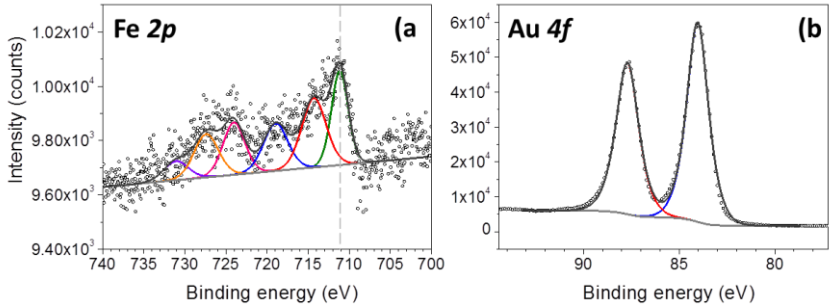


**Fig.4.7:** XPS data for the chemical grafted $Fe_4C_9$ film: Fe *2p* (a), and Au *4f* region (b) and their relative fits. The spectra were acquired using a monochromatic Al $K_\alpha$ source (1486.6eV).

The Fe*2p* and Au*4f* regions of the $Fe_4C_9$ sample are reported in fig. 4.7. As in the case of the thick film the binding energy of the Fe $2p_{3/2}$ peak is in agreement with the presence of $Fe^{3+}$. The $(A_{Au}/\sigma_{Au})/(A_{Fe}/\sigma_{Fe})$ i.e. the ratio between the Au *4f* area ($A_{Au}$), corrected by its cross-section ($\sigma_{Au}$), and the area of the Fe *2p* ($A_{Fe}$), again corrected by its relative cross-section ($\sigma_{Fe}$), was chosen as a reference for the monolayer coverage.

The exposure time of a clean Au(111) single crystal to the molecular flux was calibrated to achieve the same ratio as in the chemical grafted monolayer. A 0.85 nm film of sublimated $Fe_4Ph$, estimated from QCM data, matched the $(A_{Au}/\sigma_{Au})/(A_{Fe}/\sigma_{Fe})$ ratio of the $Fe_4C_9$ sample indicating the formation of almost monolayer coverage (table 4.2). The elemental percentage of this sample is in agreement, within the experimental error, with the expected values (table 4.2).

| | $(A_{Au}/\sigma_{Au})/(A_{Fe}/\sigma_{Fe})$ | Fe % | O % | C % |
|---|---|---|---|---|
| **Chemical grafted (1ML)** | 34.6 | – | – | – |
| **Sublimated 0.85nm (~1ML)** | 39.6 | 3.6 | 18.4 | 78.0 |
| **Sublimated 0.25 nm (<1ML)** | 141.1 | 3.1 | 18.1 | 78.8 |
| **$Fe_4Ph$ expected values** | – | 3.7 | 16.7 | 79.6 |

**Table 4.2:** XPS data relative to the samples presented in this section.

It is important to note that the area quantification in monolayer/sub-monolayer samples is made difficult by the small S/N ratio which affects the Fe *2p* signal. Moreover, the O *1s* region background is perturbed by the onset of the Au *4p 3/2* peak (fig. 4.8b). In this case the choice for the background subtraction is very critical. Indeed by using different kind of baseline, we can obtain an overestimate of about 10% (Tougaard background) or an underestimate of 15% (Linear background). Here we reported the elemental percentage obtained with the Tougaard background.

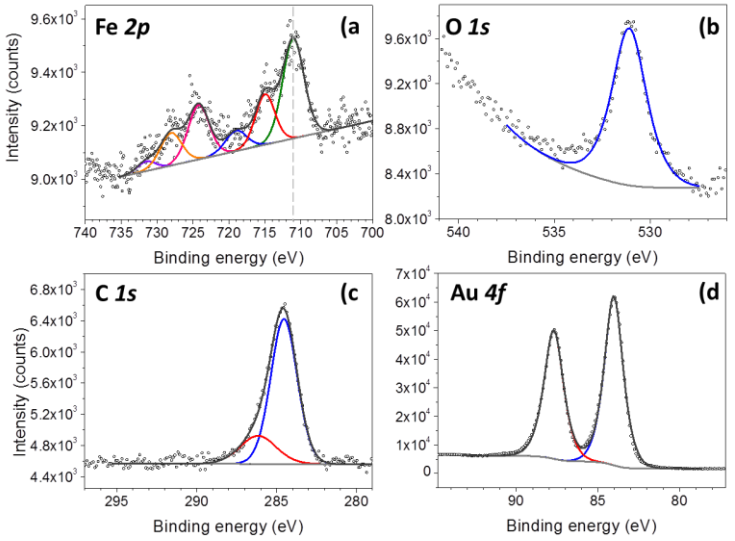


**Fig.4.8:** XPS data for 0.85 nm (~1ML)film of $Fe_4$Ph: Fe *2p* (a), O *1s* (b), C *1S* (c), and Au *4f* region (d) and their relative fits. The spectra were acquired using a monochromatic Al $K_\alpha$ source (1486.6eV).

The UPS technique is unfortunately not useful for very low coverage because the valence band of the Au substrate is still very intense and does not allow to disentangle the features of the molecule.

In order to achieve sub-monolayer coverage, which is the desired coverage for the STM investigation, a new sample was prepared with a nominal thickness of 0.25 nm. The XPS characterisation revealed a $(A_{Au}/\sigma_{Au})/(A_{Fe}/\sigma_{Fe})$ ratio significantly higher than in the previous samples, confirming the low coverage

(table 4.2). The XPS spectra show a slightly shift of the Fe $2p_{3/2}$ binding energy, probably due to the screening effect of the substrate (fig. 4.9). The elemental percentage (table 4.2) is in agreement with the data of the 0.85 nm (~1 ML) film and, within the experimental error, with the expected values.

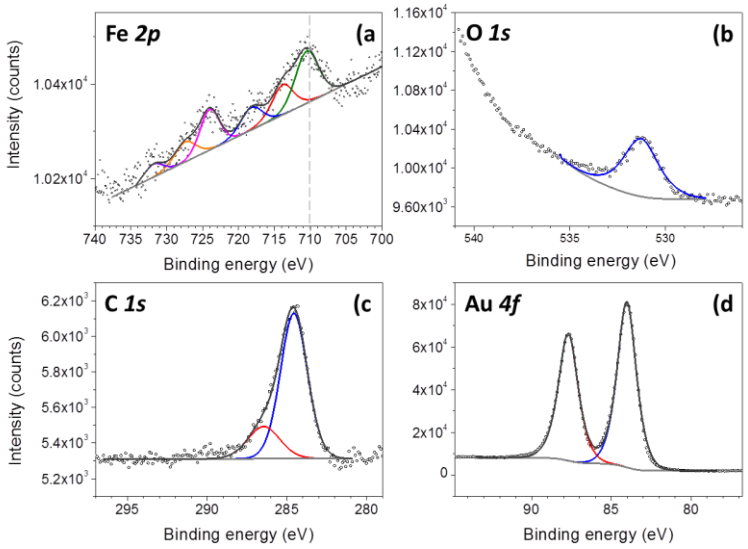


**Fig.4.9:** XPS data of 0.25 nm sub-monolayer film: Fe *2p* (a), O *1s* (b), C *1S* (c), and Au *4f* region (d) and their relative fits. The spectra were acquired using a monochromatic Al $K_\alpha$ source (1486.6eV).

The characterisations performed above have permitted the tuning of the evaporation process as planned in order to reach a very low coverage of $Fe_4Ph$ molecules. This low coverage allows to use STM for the local characterisation of the $Fe_4Ph$ molecules on surface. Moreover with the support of this STM investigation of low coverage deposition it has been possible to clarify the origin of the alteration in the elemental analysis carried out by the XPS.

## 4.4 STM characterisation of $Fe_4Ph$ sub-monolayer on Au(111)

As mentioned in section 3.1 STM investigation of SMMs on surfaces have been mostly focused on the $TbPc_2$ molecule, which is an ideal

candidate thanks to its flat shape. In fact other SMMs, such as $Mn_{12}$ and $Fe_4$ classes of SMMs, are more three-dimensional in shape and less conductive, making STM investigation of these films more difficult.

For the STM investigation we used a $Fe_4Ph$ film of about 0.25 nm estimated thickness (sub-monolayer range) sublimated on a Au(111) single crystal. After the evaporation, the sample was immediately cooled down to 35 K. The sample cooling is needed in order to prevent the molecular diffusion on the surface that would probably favour the formation of densely packed domains making difficult to get a good imaging of the molecules. It is important to stress that all the images presented here were acquired using low tunnelling current, i.e. 3 pA. Higher current values, indeed, seem to be very dangerous for the molecules which can be damaged by the tip.

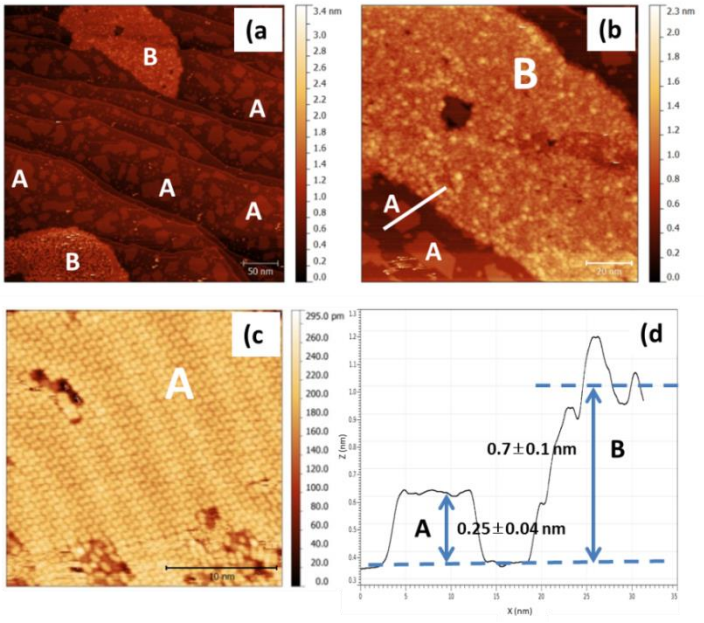


**Fig.4.10:** STM investigation of 0.25 nm sub-monolayer film. Large scale image of the surface (3pA; 2.5V; 400x400nm$^2$) (a); enlargement of the B structure (3pA; 2.5V; 120x120nm$^2$) (b); high resolution image of the A structure (3pA; 2.5V;25x25nm$^2$) (c); and the profile of the b image (d).

A large scale STM image of 0.25 nm $Fe_4Ph$/Au(111) is reported in fig. 4.10a. The image shows clearly the presence of two different

kinds of molecular domains (labelled as A and B). A close inspection of B-type domains reveals the presence of spherical objects (fig. 4.10b). On the other hand the objects forming the A-type domains seem to be very flat with a characteristic bi-lobed shape (fig. 4.10c). By looking at the profile traced in fig. 4.10b and reported in fig. 4.10d we can appreciate the different height of the two domains: 0.25±0.04 nm and 0.7±0.1 nm for A and B, respectively. It is important to note that the height of both domains is referred to the bare gold, i.e. the A and B objects are in direct contact with the surface.

Although the height estimated from STM experiments cannot be directly compared with the real height of the investigated objects, the A-type domains seem too small to be formed by intact $Fe_4Ph$ molecules. This interpretation is also supported by the bi-lobed and flat shape of the single units within the ordered domains (Fig. 4.10c). On the other hand the spherical shape of B-type objects and the greater height of their islands lead to the conclusion that $Fe_4Ph$ molecules can be associated with these domains. However, the lack of high resolution images does not allow having a better insight. In fact the formation of big, apparently disordered, islands prevents us from getting good resolution in the B-domains. The formation of such big islands can be related to a high mobility of the molecules on the Au(111) surface, which induces aggregation processes.

As far as A-type domains are concerned, they are suspected to be fragments of disintegrated $Fe_4Ph$ molecules. The contamination with fragments is particularly evident at very low coverage while it becomes practically undetectable for higher ones. Due to the very fragile nature of the polynuclear SMMs [19,20], it is possible to hypothesize different origins for the decomposition process. It could be generated during the sublimation process or simply be due to a surface-mediated fragmentation of the cluster.

Before trying to improve the morphological quality of the images of the B-domains, a test was performed in order to have some insight on the decomposition process.

### *4.4.1 Back exposure sublimation test.*

In order to shed more light on the process involved in the formation of A domains, a simple test was performed by using the sublimation geometry shown in fig. 4.11. The clean Au(111) crystal was kept in the preparation chamber for 80 minutes with the crucible at the sublimation temperature (215 °C) but without exposing the sample to the direct flux of the molecules. The surface was then investigated by STM. In large scale images (fig. 4.12a) the surface appears covered by a densely packed layer through which the corrugation of the herring bone reconstruction of the Au(111) surface can be still detected.

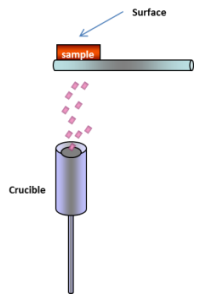


**Fig.4.11:** Back exposure geometry. The sample is not directly exposed to the molecular flux coming from the crucible.

A close inspection by STM of the surface (see the enlargement in fig. 4.12b) reveals a textured layer of small objects similar to that observed in the A-type domains of the 0.25 nm $Fe_4Ph$ sample (see fig. 4.10c). No trace of the B-type ($Fe_4Ph$) islands is revealed. This observation suggests the presence of very volatile species that can be stuck on the surface even if the sample is not directly exposed to the flux coming from the crucible. The probability that $Fe_4Ph$ molecule, as big as they are, can bounce on the chamber walls then be able to reach the sample surface is expected to be lower than for smaller, more volatile fragments.

A partial decomposition of the $Fe_4$ molecules during the sublimation process seems more likely than a surface induced fragmentation. By looking at the shape of the A objects we can speculate that they are formed by dpm-containing species. Images with objects with similar shape have been indeed reported in the study of the dissociation of a chromium tris-diketonato complex on Cu(100) surface [21].

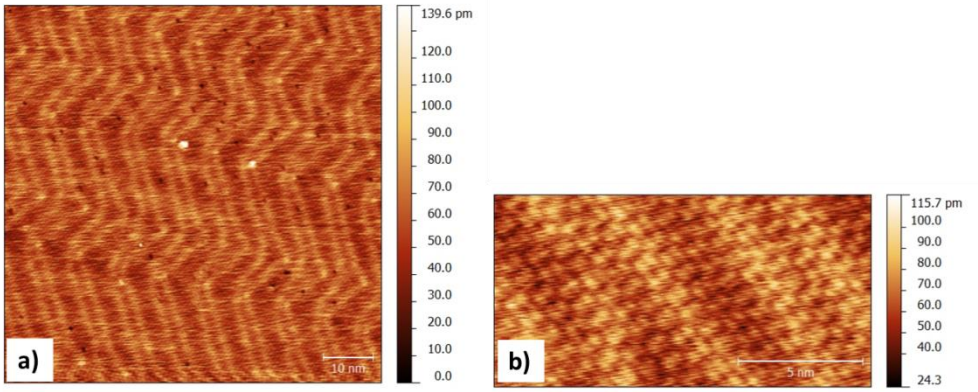


**Fig. 4.12:** Large scale STM image of the 80 min back exposed sample (3pA; 2V;110x110nm²) (a), in the enlargement (3pA; 2V;15x7.5cm²) (b) the textured layer formed by A-type molecule.

## 4.6 STM investigation on Cu(100) surface

Assuming that only domains of type B are compatible with intact $Fe_4Ph$ molecules, it is quite evident that the molecules tend to aggregate into islands, hampering the collection of high resolution images. It would be therefore advisable to reduce the mobility of the molecules. This could be achieved simply sublimating the molecules on cooled surfaces. Unfortunately our UHV system does not allow such a procedure. An alternative way is the deposition on more reactive surfaces like Cu(100). This surface is more reactive than the Au(111) one and could allow the onset of stronger molecule-surface interactions, thus reducing molecules mobility.

Again a sub-monolayer sample with similar coverage as the previous one, 0.25 nm, was prepared. The sample was cooled down to

35 K before being investigated. The STM image reported in fig. 4.13a clearly shows islands formed by well-defined spherical objects and, underneath, a wetting layer arranged in dendritic structures. As in the case of Au(111), the height of the islands measures 0.72±0.02 nm while the dendritic structures are height 0.19±0.01 nm (see profile of fig. 4.13b). The two structures were labelled as A' (0.19 nm height) and B' (0.72 nm height) in analogy to the A and B islands on Au(111) surface. It is important to point out that the B' height is referred to the A' under layer (fig 4.13b) while in the Au(111) surface is referred to the bare gold. Among the A' layer spherical objects (labelled as C') are present with a lateral dimension of 1.9±0.2 nm. A correct height estimation of the C' objects is difficult since it is not possible to discern if they lie in direct contact with the copper surface or above the A' islands. The good resolution obtained for islands of B' domains allows the estimation of the lateral dimensions of the spherical objects, i.e. 1.8±0.4 nm, which is in agreement with the expected dimension of intact $Fe_4$Ph molecules (ca. 1.7 nm). These data suggest that the molecules forming the B' regions could be intact $Fe_4$Ph molecule.

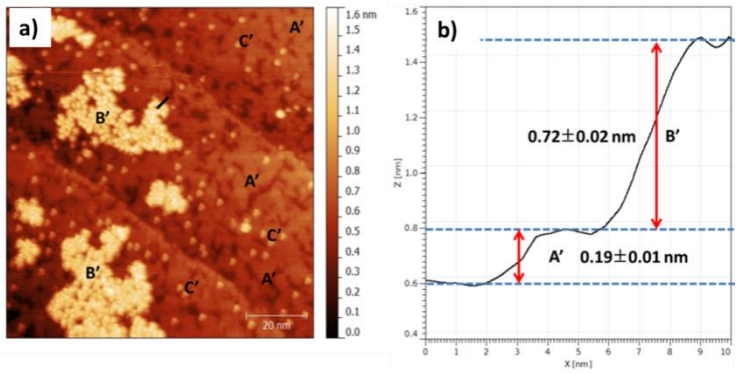


**Fig.4.13:** STM investigation of 5 min sublimated sub-monolayer film on Cu(100) substrate (3pA; 2.5V; 100x100nm$^2$) (a); and a profile of the image (b).

By comparing large scale images (400x400nm$^2$) obtained for 0.25 nm of $Fe_4$Ph on Cu(100) and Au(111), it is possible to note the B/A (B'/A') coverage ratio (molecules/contaminants) is higher for the Au(111) surface with respect to the Cu(100). The homogenous aspect

of A'-type domains suggests that B' islands are probably grown on top of the A' structures which can act as decoupling layer from the bare Cu(100) surface. These findings can be interpreted in two ways: a surface effect in the $Fe_4Ph$ molecule stability or in terms of sticking coefficients of the preformed fragments. In both cases a higher proportion of A-type domains is to be expected for Cu(100) and no unambiguous hint on surface effect can be extrapolated from this experiment. Unfortunately XPS technique cannot provide more insight. In fact, using the Al $K_\alpha$ source the Fe *2p* regions reside at the same energy of the $L_2M_{23}M_{23}$ Cu Auger peak, which overwhelms the iron components.

The presence of molecule-surface interactions are certainly related to the nature of the substrate and the investigation of the sublimation of $Fe_4Ph$ on a less reactive substrate could allow a more complete view of the phenomenon.

## 4.7 STM investigation on $Cu_2N$/Cu(100) surface

The $Cu_2N$ surface is an inert surface which has been used as electronic decoupling layer in inelastic electron tunnelling spectroscopy (IETS) studies on single atoms [22-25]. In fact the presence of the $Cu_2N$ layer allows the decoupling of magnetic impurities i.e. transition element atoms such as Fe, Mn and Co, from the valence band of the Cu(100). Although the magnetic core of the $Fe_4Ph$ molecule is expected to be decoupled from the surface by the ligands, the $Cu_2N$ surface represents a good standard for further STS investigations. The $Cu_2N$ surface can be obtained by sputtering the Cu(100) surface with $N_2$ (using 1 keV energy and 0.25 $\mu A \cdot cm^{-2}$) and annealing at 300°C for 10 min. Depending on the sputtering time different coverage of $Cu_2N$ can be achieved. However the growth of the $Cu_2N$ overlayer is self-limited to 1 ML and no multilayer of copper nitride can be obtained.

The STM image in fig. 4.14a shows a 30% coverage of $Cu_2N$ islands on Cu(100) surface. The surface is covered by square small

islands with lateral dimension of ca. 7.5 nm. This structure is due to the incommensurate nature of the $Cu_2N$ lattice (fig. 4.14b) respect to the lattice of the underlying Cu(100). The dimensions of the islands are thus a compromise between the strain and the edge energy [26–28]. By increasing the sputtering time a full layer of $Cu_2N$ can be obtained. The STM image of clean $Cu_2N$ layer is reported in fig. 4.14c.

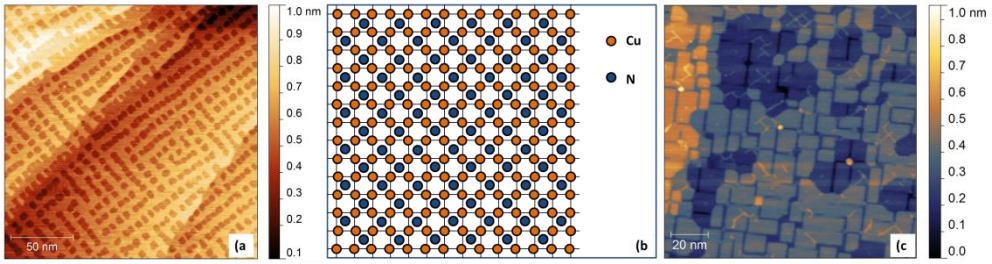


**Fig.4.14:** STM image of 30 % $Cu_2N$ coverage islands on Cu(100)(200pA; 2V; 200x200nm$^2$)(a); Atomic structure of C(2x2) $Cu_2N$ surface(b);STM image of clean $Cu_2N$ (200pA; 2V; 140x140nm$^2$)(c).

We studied a similar 0.25 nm sub-monolayer coverage of $Fe_4Ph$ also on the $Cu_2N$ surface. The large scale images of the hybrid surface (fig. 4.15a) revealed the presence of islands with ca. 0.8±0.1 nm (B'') similar to what found on Au(111) and Cu(100) surfaces. The lateral dimension of the B'' spherical objects are 1.6±0.2 nm comparable to what we measured on Cu(100) and to the real dimension of the $Fe_4Ph$ molecule (ca. 1.7 nm). By focusing on the areas between the B'' structures the presence of small objects with height of 0.28±0.02 nm (A'') was found (fig. 15b,c). It's interesting to note that on the $Cu_2N$ surface the small molecules are not able to aggregate in large domains, as observed on the other surfaces, and they present a tetra-lobed shape. The tetra-lobed shaped objects remind in some way the bi-lobed objects observed on the Au(111) surface. While in the latter case they self-assemble to form large ordered domains, in the case of $Cu_2N$ they seem to be coupled in pairs to form the tetra-lobed elements. The hole observed in the middle of the image suggests that two bi-lobed objects are coordinating something, i.e. an iron ion or a defect of the surface. As in the case of the Cu(100)

substrate the XPS technique does not provide further insight (see section 4.6).

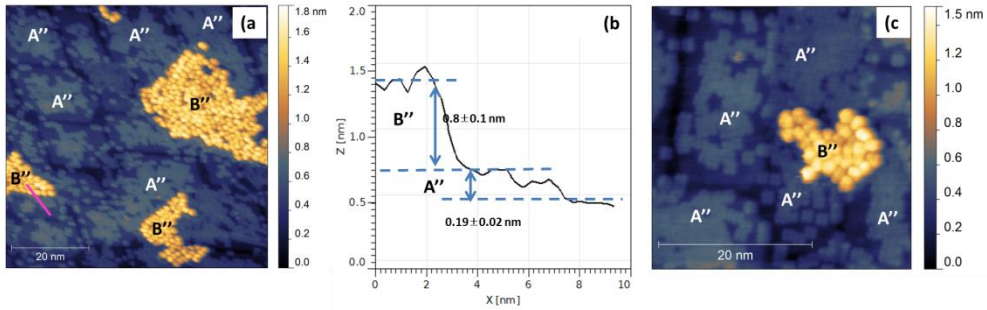


**Fig. 4.15: (a)** STM image of 2.5A of Fe4Ph on $Cu_2N$ (3pA; 2.5V; 70x70nm$^2$) **(b)**; the profile corresponding to the pink line traced in a); (c) and the enlargement where is visible the tetra-lobed shape of the A structure (3pA; 2.5V; 35x35nm$^2$).

The data presented here suggest the presence of intact $Fe_4Ph$ on surface combined also with a relevant fraction of a contaminant. In order to prove the intactness of the $Fe_4Ph$ molecules scanning tunnelling spectroscopy (STS) was employed (see section 2.8.3). The measurements were performed on a different UHV-STM system which was designed to achieve the high performance required for the study of the inelastic electron tunnelling spectroscopy (IETS).

## 4.8 STS and IETS measurements

The STS measurements were carried out at the Max Planck Research Group – Dynamics of Nanoelectronic Systems in Hamburg. Thanks to the collaboration with Dr. S. Loth's group I have had the opportunity to work for three weeks in their laboratory. We obtained encouraging first results and more detailed experiments are continued now. Being able to perform low temperature STS measurements on a complex and fragile molecule like $Fe_4$ is an important achievement in itself. In this section the first spin excitation spectra consistent with intact $Fe_4$ molecules and their preliminary analysis will be presented. The UHV-STM in Hamburg is specifically designed to perform inelastic electron tunnelling spectroscopy (IETS) for the study of the electronic and magnetic properties of single atoms, nanostructures and molecules.

The STM, equipped with a pumped $^3$He cooling system, can perform measurements down to 0.4 K allowing the study of the $Fe_4$Ph molecule below its blocking temperature. It is also equipped with a vectorial superconductive magnet, which allows the application of a magnetic field up to 90 kOe along the STM junction direction and up to 20 kOe in an arbitrary direction.

The d(I)/d(V) spectra were acquired using a lock-in detection of an applied bias modulation. In this STM the tip is grounded and the potential is applied to the sample, it is therefore opposite to the Omicron STM instrument (section 2.9.3). For the sample preparation we adapted our experimental sublimation setup (see section 2.2) to their UHV system. In order to avoid the formation of molecular domains and to freeze the single molecules on the surface the sublimation process was carried out with the sample kept at 4 K. We employed the $Cu_2N$ surfaces as substrate because it does not allow the formation of large islands and the B'' objects lay in direct contact with the bare surface. The analysis of the STM images reveals that both the A'' and B'' molecules are present on the surface. We focused our investigation only on the B'' molecules which, as demonstrated in the previous chapters, can be considered $Fe_4$Ph candidates.

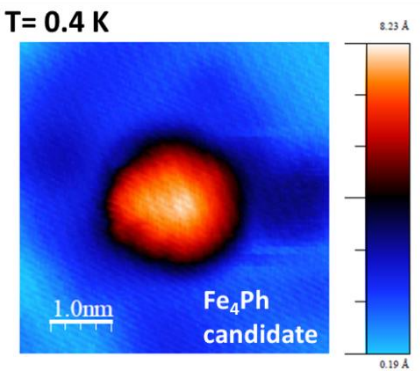


**Fig.4.16:** STM image of single B'' molecule sublimated on $Cu_2N$ surface. The image was acquired at 0.4 K (3pA; 2.0V; 5x5nm$^2$).

The STM image of isolated B'' molecules, acquired with both STM tip and sample at 0.5 K, is reported in fig. 4.16. Their apparent

height and lateral dimensions are in agreement with those revealed in the previous experiment. On such candidates several attempts were carried out to look for the HOMO/LUMO features in the differential conductance curves acquired on top of the molecules. These measurements were partially hampered by the molecular fragility i.e. molecular fragmentation during the bias sweep (few V), and no clear data were recorded to be compared with the experimental and theoretic density of states.

Our study was then focused on a small sweep range (few mV) centred in zero bias, which was disrupting for the molecules. In this energy range inelastic tunnelling processes related to spin excitation transitions can be detected. The tunnelling process can in fact occur following two pathways: by elastic and by inelastic tunnelling. In the former case the electron does not interact with the environment while in the inelastic process the electron exchanges energy during the tunnelling process through the molecule.

The inelastic tunnelling process can be employed to achieve information on the energy levels of the inspected system. In fact, it has been first used in planar junction to study vibrational excitations in molecules [29–31]. Then the STM technique has enabled the study of spin excitation in single magnetic metal atoms, nanostructures [22,32–34], and SMMs [35].

To briefly explain the main concepts of the spin excitation process let us consider a spin system inside the tunnelling gap i.e. between the tip and the surface (fig. 4.17). The green arrows in fig.4.18 represent the elastic tunnelling. This tunnelling channel is always available, regardless of applied bias, provided there are filled states in one electrode and empty state in the opposite electrode at the same energy. However, when electrons possess enough energy they can interact with the local spin promoting a transition within the sublevels of the spin and still reach empty states (fig. 4.17b). This process constitutes the inelastic tunnelling phenomenon and it can be considered as an additional conduction channel. Thus, when the applied bias matches the required energy for the spin transition to be excited the inelastic channel becomes available. This leads to an

increase of the conductance of the system which is now formed by both the elastic and inelastic conduction channels. The spin excitation process is thus detected as a step in the differential conductance. It is important to note that the threshold voltages at which the steps are observed corresponds to the energy of the excitations.

In fig. 4.18a is reported the differential conductance d(I)/d(V) curves acquire on the bare $Cu_2N$ substrate and on B'' molecule in zero magnetic field. As expected the curve on $Cu_2N$ is flat while the one recorded on the molecule is characterised by two steps close to the zero bias value, which look like a negative peak (fig. 4.18a). These features can be attributed the presence of spin excitation process. At 0.5 K the ground state of the double well $|S, m_s\rangle$=$|5, \pm5\rangle$ is selectively populated and the inelastic process excite the spin levels of the molecule to the $|5, \pm4\rangle$ states (fig. 4.18b). The features in the differential curve of the B'' molecule is indicative of inelastic tunnelling process onset above a bias of absolute value ca. 0.5 mV. This is in agreement with the expected calculated energy involved in $|5, \pm5\rangle$ to $|5, \pm4\rangle$ transition of $Fe_4Ph$, i.e. 0.47 meV.

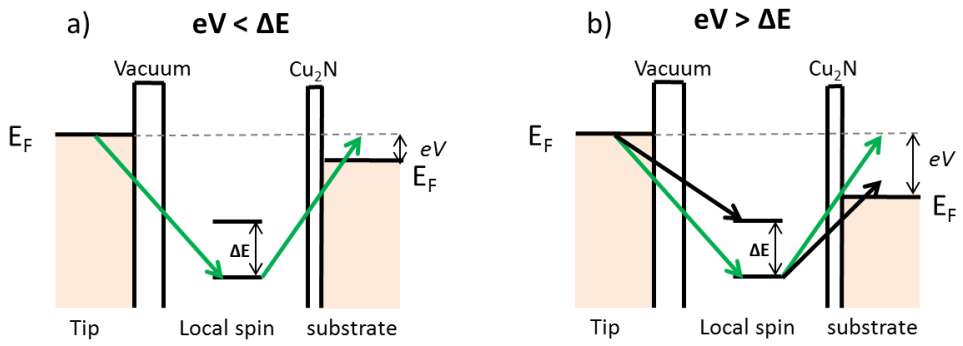


**Fig.4.17:** Scheme of the tunnelling processes; When the electron energy, i.e. the applied bias *eV,* is less than the energy required for the molecular transition only the elastic process is present (green arrows)(a); on the contrary when the electrons energy is enough to excite the spin system the inelastic tunnelling can occur (black arrows) opening a new tunnelling channel and increasing the differential conductance.

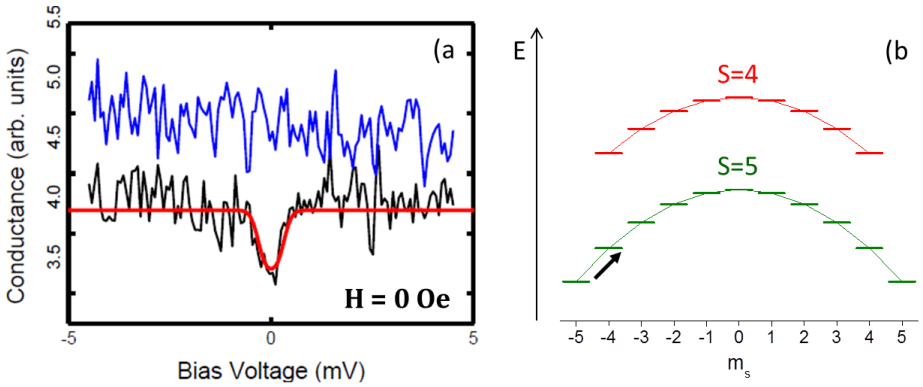


**Fig.4.18:** IETS measurement on top of B'' molecule (black) and the same measurement on bare $Cu_2N$ surface (blue) acquired using lock-in detection at 768 Hz and 100 μV amplitude modulation and calculated spectra (red)(a). $Fe_4Ph$ levels scheme (b), at 0.4 K the system resides in the ground state $|\mathbf{5},\pm\mathbf{5}\rangle$and the inelastic tunnelling can excite the molecule to the $|\mathbf{5},\pm\mathbf{4}\rangle$ states; the black arrow indicates the possible excitation which obeys to the spin selection rules $\Delta S=0, \pm1$ and $\Delta m_s=0, \pm1$. Graph in panel (a) courtesy of Dr. J. Burgess, Hamburg.

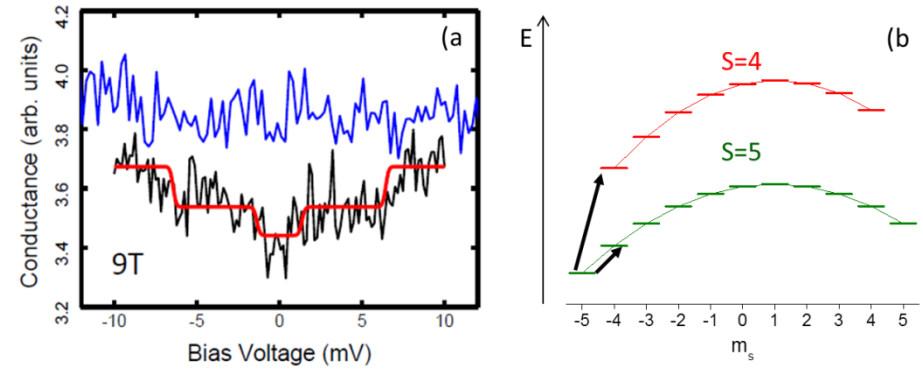


**Fig.4.19:** IETS measure on top of B'' molecule (black) and the same measure on bare $Cu_2N$ surface (blue) acquired using lock-in detection at 768 Hz and 100 μV amplitude modulation and calculated spectra (red)(a). Simplified $Fe_4Ph$ levels scheme (b) considering the field applied along the molecular easy axis. The black arrows indicate the possible excitation which obeys to the spin selection rules $\Delta S=0, \pm1$ and $\Delta m_s=0, \pm1$. Graph in panel (a) courtesy of Dr. J. Burgess, Hamburg.

These measurements clearly demonstrate the capability of the technique to provide fine details on the electronic structure of the deposited species at the single-molecule level. However, the fragile nature of the $Fe_4$ molecules makes the IETS experiment rather challenging. The presence of this spin excitation in fact was not

consistently detected on every candidate and a larger set of data must be acquired to confirm these preliminary results.

The experiment was repeated applying 90 kOe magnetic field normal to the sample surface. The magnetic field can be taken in account in the Hamiltonian description introducing the Zeeman term which removes the degeneracy of the $|5, \pm 5\rangle$ states. The spectra acquired are reported in fig. 4.19a. The measure was performed using a larger bias range compared to the zero field measurement. This allowed the observation of four steps: two at ca. 1 mV and two at ca. 7 mV absolute bias values.

The higher energy steps could be associated to a process involving a transition from the $S$=5 ground state to the first excited total spin state, characterised by $S$=4, as depicted in fig. 4.20b. This feature was also present in zero magnetic field measurements. It is however important to notice that this spectral feature at higher bias showed a variability significantly larger than the one observed at low bias. Although the different orientation of the $Fe_4$ molecules on the substrate could be at the origin of the differences observed under applied magnetic field, the residual inconsistencies suggest that other factors, like the chemical instability of the molecules in the experimental conditions, must be taken into account. Further investigations are therefore needed for a reliable assignment of these spectral features.

The red spectra in fig. 4.18 and 4.19 show the expected spin excitation spectra for intact $Fe_4$ molecules for comparison. The conductance spectra were simulated using the $Fe_4$ spin anisotropy parameters from ref. [7] under the assumption that tunnelling interaction happens with the Fe atoms individually. The calculations were performed by Dr. S. Loth using scattering theory in 1st Born approximation. The transition intensities were computed using an interaction Hamiltonian:

$$H = \sigma \cdot S + U \qquad (5)$$

where $\sigma$ is the electron spin, $S$ the spin of the Fe atoms and $U$ a spin independent scattering term [36]. This operator acts on the product states of electron and molecule spin. In this way the selection rules are imposed by energy and angular momentum conservation; spin-dependent conduction channels can be accounted for.

Although only a preliminary characterisation of the spin excitation of $Fe_4Ph$ molecules through IESTS has been possible during my stay in Hamburg, the results are rather encouraging, confirming that objects consistent with intact and isolated $Fe_4$ molecules can be detected and addressed at the $Cu_2N$ surface. Moreover the observation of spectroscopic features in agreement with the ones predicted assuming the Spin Hamiltonian parameters of $Fe_4$ molecules in the crystalline phase suggests that the magnetic features of this SMM are very robust. These novel results corroborate the observation of magnetic bistability in self-assembled monolayers by XMCD, or the detection of spectroscopic features in the conductivity inside nano-gap electrodes [37-39] and open the fascinating perspective of detecting the magnetic bistability, and related memory effect, at the single molecule level by using scanning-probe microscopy techniques.

## References


[1] D. Gatteschi, R. Sessoli, and V. Jacques, Oxford Univ. Press (2006).

[2] A. L. Barra, A. Caneschi, A. Cornia, F. Fabrizi de Biani, D. Gatteschi, C. Sangregorio, R. Sessoli, and L. Sorace, J. Am. Chem. Soc. **121**, 5302 (1999).

[3] A. Cornia, A. C. Fabretti, P. Garrisi, C. Mortalò, D. Bonacchi, D. Gatteschi, R. Sessoli, L. Sorace, W. Wernsdorfer, and A.-L. Barra, Angew. Chemie **116**, 1156 (2004).

[4] A. Cornia, A. . Fabretti, P. Garrisi, C. Mortalò, D. Bonacchi, R. Sessoli, L. Sorace, A.-L. Barra, and W. Wernsdorfer, J. Magn. Magn. Mater. **272-276**, E749 (2004).

[5] S. Accorsi, A. Barra, A. Caneschi, G. Chastanet, A. Cornia, A. C. Fabretti, D. Gatteschi, C. Mortalo, E. Olivieri, F. Parenti, P. Rosa, R. Sessoli, L. Sorace, W. Wernsdorfer, and L. Zobbi, J. Am. Chem. Soc. **128**, 4742 (2006).

[6] L. Bogani and W. Wernsdorfer, Nat. Mater. **7**, 179 (2008).

[7] M. Mannini, F. Pineider, P. Sainctavit, C. Danieli, E. Otero, C. Sciancalepore, A. M. Talarico, M.-A. Arrio, A. Cornia, D. Gatteschi, and R. Sessoli, Nat. Mater. **8**, 194 (2009).

[8] M. Mannini, F. Pineider, C. Danieli, F. Totti, L. Sorace, P. Sainctavit, M. Arrio, E. Otero, L. Joly, J. C. Cezar, a Cornia, and R. Sessoli, Nature **468**, 417 (2010).

[9] M. J. Rodriguez-Douton, M. Mannini, L. Armelao, A.-L. Barra, E. Tancini, R. Sessoli, and A. Cornia, Chem. Commun. (Camb). **47**, 1467 (2011).

[10] L. Margheriti, M. Mannini, L. Sorace, L. Gorini, D. Gatteschi, A. Caneschi, D. Chiappe, R. Moroni, F. B. de Mongeot, A. Cornia, F. M. Piras, A. Magnani, and R. Sessoli, Small **5**, 1460 (2009).

[11] L. Margheriti, PhD Thesis (2010).

[12] T. Yamashita and P. Hayes, Appl. Surf. Sci. **254**, 2441 (2008).

[13] L. Rigamonti, M. Piccioli, L. Malavolti, L. Poggini, M. Mannini, F. Totti, B. Cortigiani, A. Magnani, R. Sessoli, and A. Cornia, Inorg. Chem. **52**, 5897 (2013).

[14] C. J. Mundy, F. Mohamed, F. Schiffman, G. Tabacchi, H. Forbert, W. Kuo, J. Hutter, M. Krack, M. Iannuzzi, M. McGrath, M. Guidon, T. D. Kuehne, T. Laino, J. VandeVondele, and V. Weber, CP2K Softw. Packag. (n.d.).

[15] S. Grimme, J. Antony, S. Ehrlich, and H. Krieg, J. Chem. Phys. **132**, 154104 (2010).

[16] Y. Zhang and W. Yang, Phys. Rev. Lett. **80**, 890 (1998).

[17] S. Goedecker, M. Teter, and J. Hutter, Phys. Rev. B **54**, 1703 (1996).

[18] M. Ernzerhof and G. E. Scuseria, J. Chem. Phys. **110**, 5029 (1999).

[19] S. Voss, M. Burgert, M. Fonin, U. Groth, and U. Rüdiger, Dalton Trans. **7**, 499 (2008).

[20] M. Mannini, P. Sainctavit, R. Sessoli, C. Cartier dit Moulin, F. Pineider, M.-A. Arrio, A. Cornia, and D. Gatteschi, Chem. Eur. J. **14**, 7530 (2008).

[21] S. E. Grillo, H. Tang, C. Coudret, and S. Gauthier, Chem. Phys. Lett. **355**, 289 (2002).

[22] C. F. Hirjibehedin, C. P. Lutz, and A. J. Heinrich, Science **312**, 1021 (2006).

[23] A. F. Otte, M. Ternes, K. von Bergmann, S. Loth, H. Brune, C. P. Lutz, C. F. Hirjibehedin, and A. J. Heinrich, Nat. Phys. **4**, 847 (2008).

[24] S. Loth, K. von Bergmann, M. Ternes, A. F. Otte, C. P. Lutz, and A. J. Heinrich, Nat. Phys. **6**, 340 (2010).

[25] S. Loth, M. Etzkorn, C. P. Lutz, D. M. Eigler, and A. J. Heinrich, Science **329**, 1628 (2010).

[26] T. Choi, C. Ruggiero, and J. Gupta, Phys. Rev. B **78**, 035430 (2008).

[27] F. M. Leibsle, S. S. Dhesi, S. D. Barrett, and A. W. Robinson, Surf. Sci. **317**, 309 (1994).

[28] F. Komori, S. Ohno, and K. Nakatsuji, J. Phys. Condens. Matter **14**, 8177 (2002).
[29] P. K. Hansma and J. Kirtley, Acc. Chem. Res. **11**, 440 (1978).
[30] R. Jaklevic and J. Lambe, Phys. Rev. Lett. **17**, 1139 (1966).
[31] W. H. Weinberg, Annu. Rev. Phys. Chem. **29**, 115 (1978).
[32] A. J. Heinrich, J. A. Gupta, C. P. Lutz, and D. M. Eigler, Science **306**, 466 (2004).
[33] C. F. Hirjibehedin, C.-Y. Lin, A. F. Otte, M. Ternes, C. P. Lutz, B. A. Jones, and A. J. Heinrich, Science **317**, 1199 (2007).
[34] S. Loth, S. Baumann, C. P. Lutz, D. M. Eigler, and A. J. Heinrich, Science **335**, 196 (2012).
[35] S. Kahle, Z. Deng, N. Malinowski, C. Tonnoir, A. Forment-Aliaga, N. Thontasen, G. Rinke, D. Le, V. Turkowski, T. S. Rahman, S. Rauschenbach, M. Ternes, and K. Kern, Nano Lett. **12**, 518 (2012).
[36] S. Loth, C. P. Lutz, and A. J. Heinrich, New J. Phys. **12**, 125021 (2010).
[37] H. Heersche, Z. de Groot, J. Folk, H. van der Zant, C. Romeike, M. Wegewijs, L. Zobbi, D. Barreca, E. Tondello, and A. Cornia, Phys. Rev. Lett. **96**, 206801 (2006).
[38] A. S. Zyazin, J. W. G. van den Berg, E. A. Osorio, H. S. J. van der Zant, N. P. Konstantinidis, M. Leijnse, M. R. Wegewijs, F. May, W. Hofstetter, C. Danieli, and A. Cornia, Nano Lett. **10**, 3307 (2010).
[39] A. S. Zyazin, H. S. J. Van Der Zant, M. R. Wegewijs, and A. Cornia, Synth. Met. **161**, 591 (2011).